Correlation between color changes in Jupiter's storm "Oval BA", cloud heights and ultraviolet exposure

Tejoram Vivekanandan, Coimbatore Institute of Technology

Mentor: Glenn Orton, Jet Propulsion Laboratory

Co-Mentor: Thomas Momary, Jet Propulsion Laboratory

Abstract

Oval BA is the second largest second largest anti-cyclonic vortex on Jupiter's surface, the largest being, the Great Red Spot. Oval BA formed in 2000 and followed quasi-periodic color changes over the years. Its initial white color started to change on November 2005 and became completely red on December 2005. Then, the red color was sustained for more than a decade. On July 2018, it was observed that the red color was fading. It turned to completely white on December 2018 and stayed white for a couple of years. In recent observations in 2021, the Oval BA is changing its color to a faint red or pink again. To determine the correlation between the color change, the altitude and ultraviolet exposure of the storm's particles, near-infrared images of Jupiter with Oval BA present were examined. After some calibration and preprocessing the images during red, white and the transition phase were compiled for different wavelengths. The reflectivity of the vortex at each wavelength was corrected for dependence on angles of emission and incident sunlight using the Minnaert function. Results confirm a behavior that is consistent with a change in altitude of particles between the red and white epochs.

Introduction

Jupiter is the largest planet in the solar system. There is no solid surface on Jupiter. The atmosphere is filled various cyclonic and anti-cyclonic vortices i.e. storms rotating in the same or in the opposite direction as the planet. One such anti-cyclonic storm is Oval BA, located in Jupiter's southern hemisphere. The latitude of the storm is relatively constant, near 33°S planetocentric latitude, but the longitude of the vortex is not constant because of drifting in the turbulent atmosphere in Jupiter. The size of Oval BA is large enough to comfortably engulf the Earth. Oval BA formed in 2000 as a result of the merger of three white smaller storms. It was the same white color of the smaller storms. However, in December 2005, Oval BA was observed to have changed colors from white to red during a time it was not observable due to proximity to the sun. It stayed this color for a little more than a decade [1]. In July 2018, observers noted that Oval BA's red color was fading [2]. By December 2018, after Jupiter's solar conjunction, it was observed that Oval BA had once again become white [2]. The purpose of this study is to determine whether these color changes are associated with any change of altitude of the particles within Oval BA.

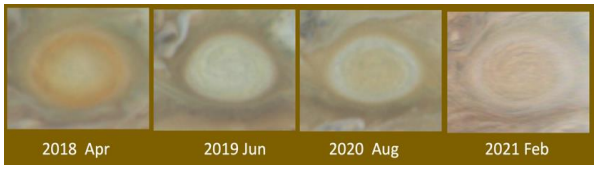

Figure 1. Changes of color of the anticyclone Oval BA. (Left) Red color Oval BA observed on April 2018. (Middle Left) White color Oval BA observed on June 2019. (Middle Right) Transition of white to Pink Oval BA observed on August 2020. (Right) Pink color Oval BA observed on February 2021.

Methods

Image collection and calibration

This project collects images from the SpeX instrument at NASA's InfraRed Telescope Facility (IRTF) and the Near-InfraRed Imager (NIRI) at the Gemini North Telescope. Both facilities are at the summit of the ~14,000 foot Maunakea, Hawaii. The images provided by both instruments cover the spectral range between 1.58 and 2.26 µm. Any unprocessed image in IR observation would be highly affected by sky background emission. This situation is similar to trying to view stars during the daylight at visible wavelengths. To avoid this we would use the Nodding technique, which subtracts a nearby sky background image from the Jupiter image. Figure 2 represent examples of the Nodding technique.

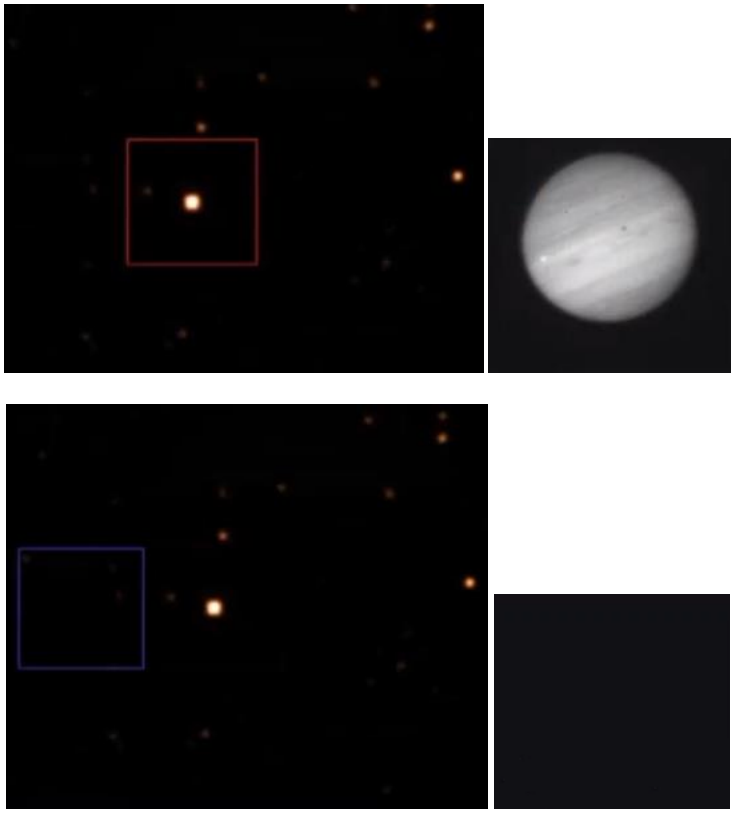

Figure 2. (Top) On source image. (Bottom) Off source image. The top right image shows Jupiter while on source. The bottom right image shows background sky while off source.

Image Compilation and Sorting

Jupiter was imaged using several discrete filters at near-infrared wavelengths sensitive to reflected sunlight from clouds at various levels in Jupiter's upper troposphere and lower stratosphere. Images were selected in which Oval BA was visible. The selected images were taken at various wavelengths and include epochs when Oval BA is visibly red, white, and the transition the follows.

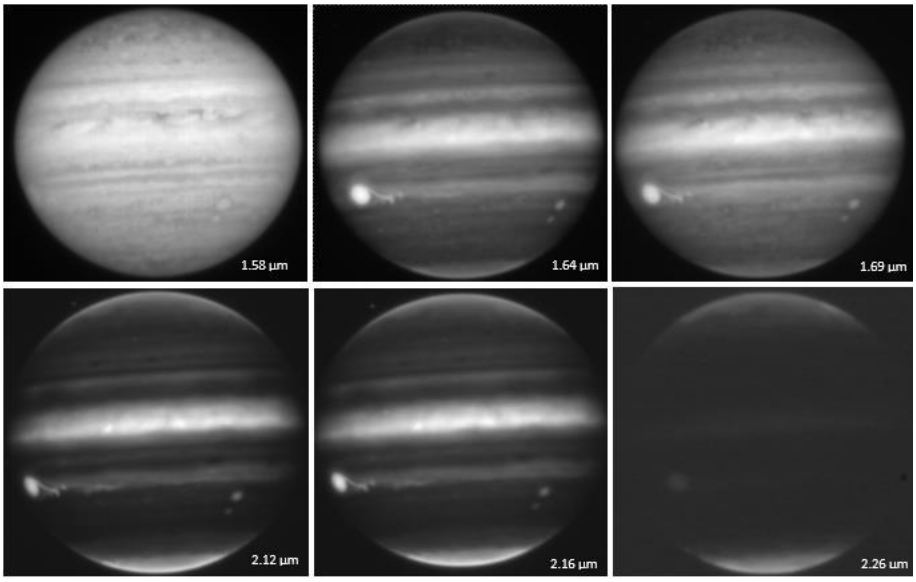

Figure 3. Images taken using the SpeX instrument's "Guide Dog" camera on Jun 3, 2019 at various wavelengths. Oval BA is recognizable as the brighter oval near the "4-o'clock" position of these images.

After this compilation process, the images are sorted based on their respective wavelengths as a function of time to determine if there are any visible changes present in Oval BA's surroundings or morphology. The SpeX filters in which images are compiled include the short absorption band of methane (1.58 µm), iron II (1.64 µm), long absorption bands of methane (1.69 µm), hydrogen 1-0 (2.12 µm), bracket gamma (2.16 µm), and continuum-K (2.26 µm). The NIRI filters in which images are compiled include the short and long absorption bands of methane, bracket gamma, hydrogen, H2O-ice (2.05 µm), and methane-ice (2.28µm). Figure 3 shows examples of IRTF SpeX images with Oval BA present. Subsequently, these images are converted into cylindrical maps.

Central-Meridian Plots

Next, central-meridian strips are extrapolated from the previously created cylindrical maps in order to check the consistency of the image set's reflectivity and verify whether or not some discrete feature such as the Great Red Spot or a bright satellite had made the initial process of calibration (by averaging over the Earth-facing hemisphere) inaccurate.

To make the central meridian plots, images are grouped together by wavelength, and an input file of relevant images is created for each wavelength. Next, central-meridian strips are taken from the cylindrical maps and are plotted in a line graph. If any of the images have central meridian strips that deviate greatly from the norm, these images are taken out of this input file and added to a new input file that consists of all the outliers for the wavelength. Finally, an average central-meridian strip that excludes the outlier data is drawn onto the plot. The outlier images are then re-adjusted and re-calibrated in order to be more consistent with the mean and are added back into the original input file to create a more accurate central-meridian plot.

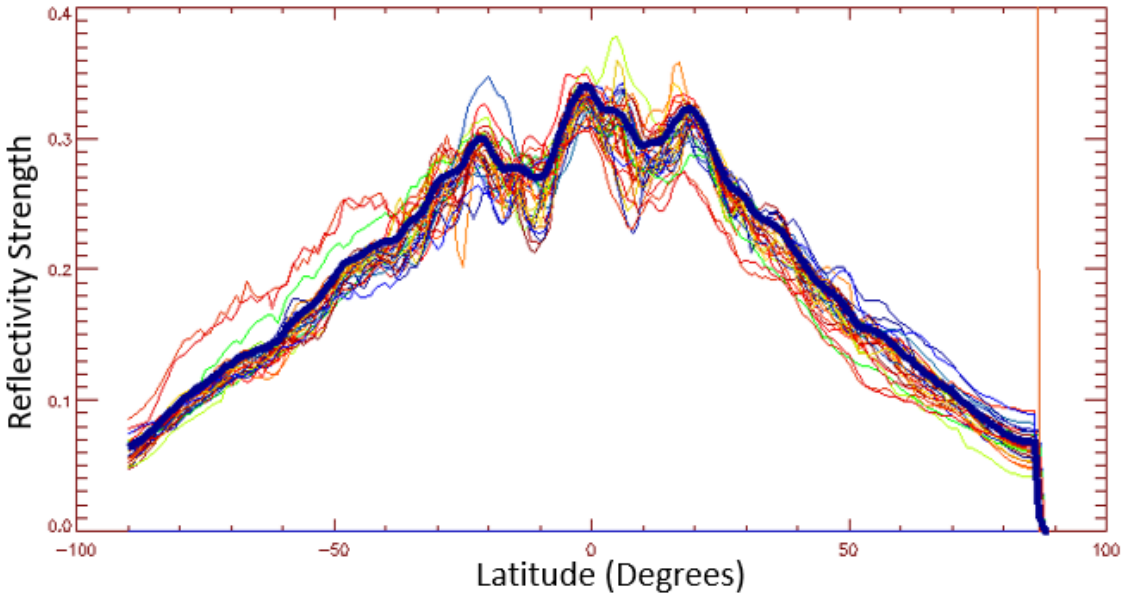

Figure 4. A composite central meridian plot of images at a wavelength of 1.58 microns.

The Minnaert Function

The dependence of the observed reflectivity from a planet's location on the incidence and emission angles can be approximated using the Minnaert function [4]. This empirical law was first introduced by Marcel Minnaert in 1941. For an observation at a specific wavelength, one can approximately calculate the observed reflectivity (I/F) as:

$$\frac{I}{F} = \left(\frac{I}{F}\right)_0 \mu_0^k \mu^{k-1} \qquad \text{(Eq. 1)}$$

where $\left(\frac{I}{F}\right)_0$ is the nadir-viewing reflectivity of the selected point, *k* is the limb-darkening parameter, μ is the cosine of the emission angle at that point, and $\mu_0$is the cosine of the solar incidence angle at the same point [4]. After taking the logarithms of both sides of this equation and performing algebraic manipulations, the equation can be rewritten as:

$$ln\left(\mu\frac{I}{F}\right) = ln\left(\frac{I}{F}\right)_0 + k\ ln(\mu\mu_0) \quad \text{(Eq. 2)}$$

Using this form of the equation, it is possible to emulate a linear regression line in slope intercept form ($y = mx + b$) where $y = ln\left(\mu\frac{I}{F}\right)$, $m = k$, $x = (\mu\mu_0)$, and $b = ln\left(\frac{I}{F}\right)_0$. Thus, it is possible to fit the Minnaert parameters $\left(\frac{I}{F}\right)_0$ and k using a least-squares fit on a set of $ln\left(\mu\frac{I}{F}\right)$ as a function of $(\mu\mu_0)$ [4]. It is this linearized form of the Minnaert function that is plotted in the figures below.

After final-stage calibrations have been completed, images in which Oval BA was barely visible, blurry, or too close to either limb of the planet are taken out of the datasets to improve the overall quality of the data being considered. First, using cylindrical maps the coordinates of the center of Oval BA are found. Next, with the coordinates averaged version of the I/F value is computed. The averaged version would produce more reliable values rather the single pixel computation method by increasing the stability. The kernel size to compute the average value totally depends on the size of the Oval BA in the respective image. The distance from the Earth to the Jupiter is on constant change caused by planetary motion. As our observations were made on ground-based telescopes, it is important that we need to consider the change in distance. Figure 5 shows the distance between the Earth and the Jupiter measured in astronomical unit over the years. Obviously, with change in distance, size of Oval BA in the image changes irrespective of change in actual size of the Oval BA. Thus, in our computation the kernel size is fixed with respect to the distance on date of observation.

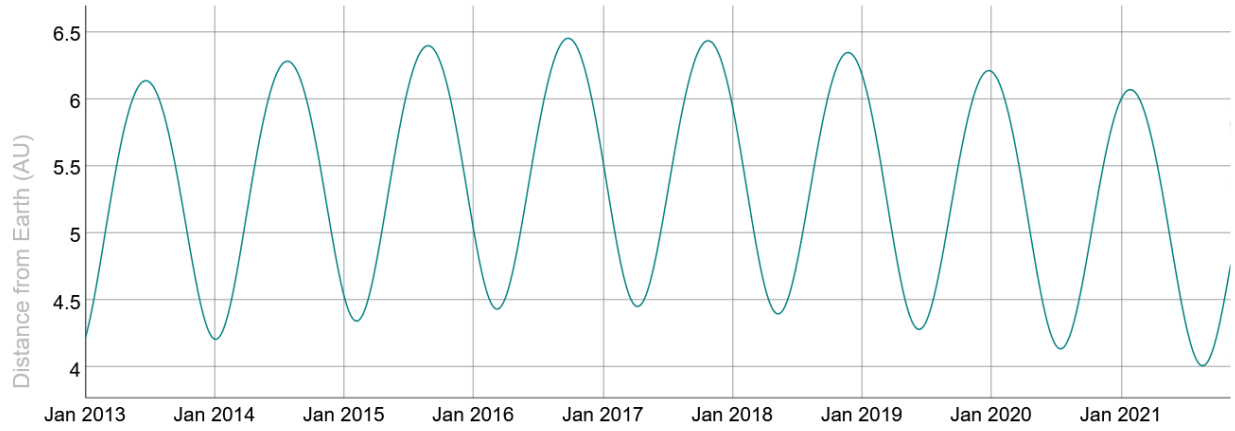

Figure 5. Distance of Jupiter from earth measured in astronomical unit (AU).

Similarly, μ and μ_0 values are determined using each cylindrical map's respective *.mu and *.mu0 files. Also, I/F values are determined at longitudes on either side of Oval BA, which we termed as West I/F and East I/F. These values are then documented in a separate table characterized by the image's wavelength and epoch ("red" or "white").

After these values are compiled, they are plotted. Next, a line of best fit is generated, and the uncertainty of the data is recorded.

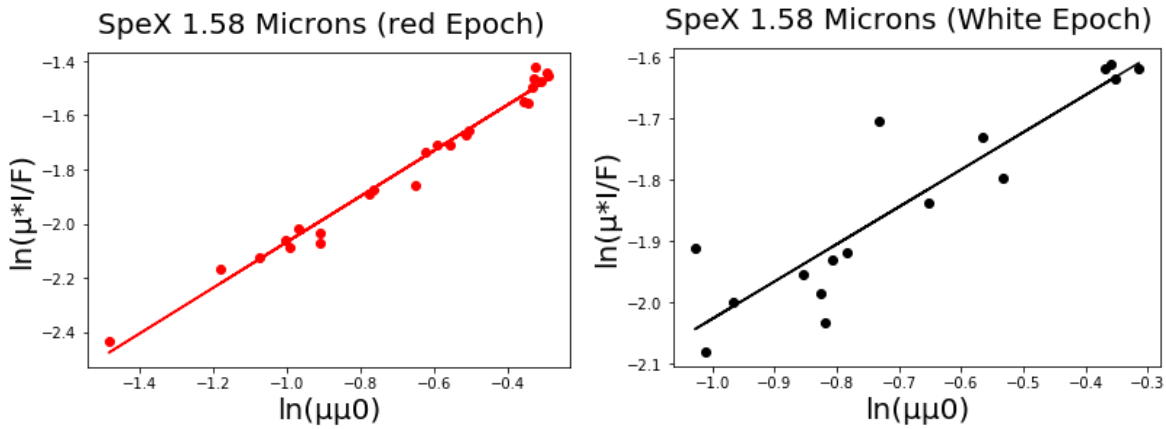

Figure 6. (Left) A plot of the reflectivity (y-axis) as a function of emission and incident angle cosines (x-axis) during the red epoch of Oval BA in SpeX observations.(Right) A plot of the reflectivity (y-axis) as a function of emission and incident angles (x-axis) during the white epoch of Oval BA in SpeX observations.

These two plots are then combined to see if there exists a different pattern of reflectivity values for the two different epochs of Oval BA. This process is repeated for each of the SpeX and NIRI filters.

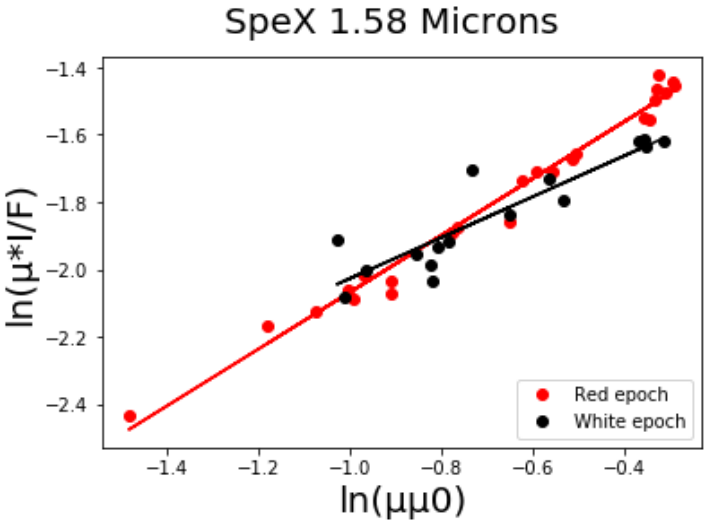

Figure 7. A plot of the reflectivity as a function of emission and incident angles of both the red and white epochs of SpeX observations overlaid against each other.

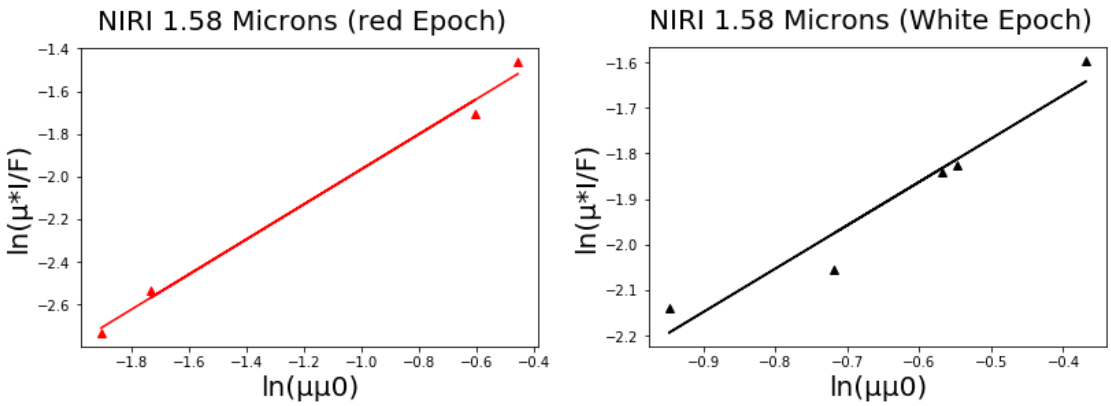

Figure 8. Plots of the reflectivity (y-axis) measured for NIRI images as a function of emission and incident angles (x-axis): Left during the red epoch of Oval BA: Right during the white epoch of Oval BA

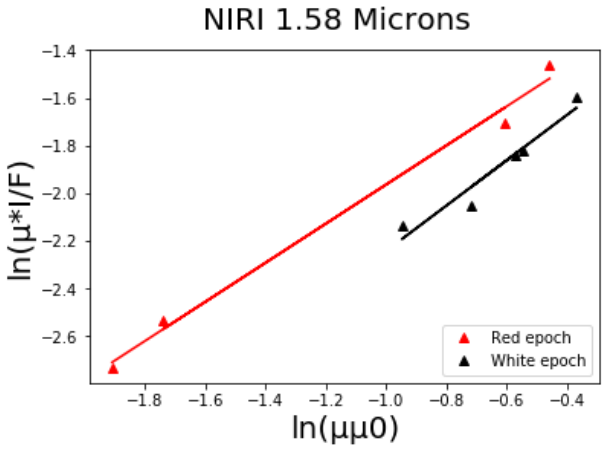

Figure 9. A plot of the reflectivity as a function of emission and incident angles of both the red and white epochs of NIRI observations overlaid against each other.

In addition, SpeX and NIRI filters that cover the same wavelength are combined to see if their reflectivity patterns are consistent during both epochs. At the wavelengths that contain both SpeX and NIRI observations, the combined data of the red and white epochs are over-plotted for further comparisons between the two epochs.

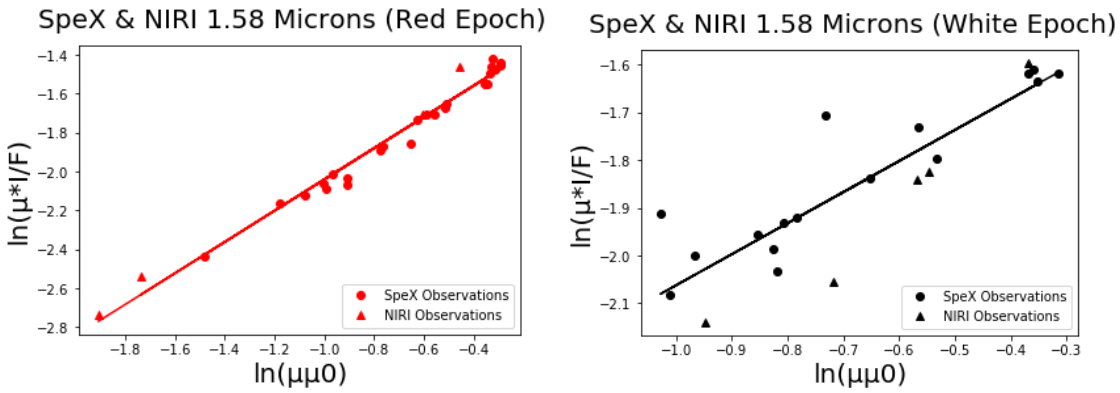

Figure 10. (Left) A combined plot of SpeX and NIRI observations in the red epoch taken using the methane short band filter (1.58 μm). (Right) A combined plot of SpeX and NIRI observations in the white epoch taken using the methane short band filter (1.58 μm).

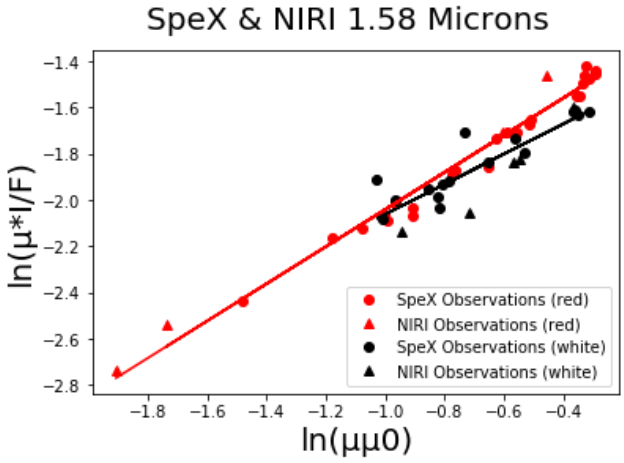

Figure 11. A plot of the reflectivity as a function of emission and incident angles of both the red and white epochs of SpeX and NIRI observations overlaid against each other using the methane short band filter (1.58 μm).

Using the uncertainties for the slope and y-intercept for the lines of best fit for both epochs, it is possible to create a confidence interval for each epoch's observed reflectivity to view the difference in I/F values. To do this, the largest product of a pair of μ and μ0 values in the epoch is selected to ensure that that specific point on the x-axis ((μμ0)) contains overlapping data for both epochs without fear of extrapolation. This value of μ, in addition to the confidence intervals for the slope and y-intercept for each epoch, can be substituted into the linear regression form of the Minnaert equation. The confidence interval for the observed reflectivity is achieved by solving for I/F using this equation. After calculating the confidence interval of the reflectivity for both the red and white epochs, it is possible to compare these values to see if there is enough certainty that a change in reflectivity occurred when Oval BA went through its transformation of red to white.

Results

Our goal was to determine whether there were any changes in the properties of particles in the atmosphere, diagnosed by changes in their near-infrared reflectivity, that could be diagnostic of changes in the particle properties, particularly altitude. If the reddening of Oval BA particles is the result of solar ultraviolet irradiation that increases with particle altitude, then is the return to white-colored particles the result of drop in the particle altitude? This would be diagnosed by lower reflectivity in spectral regions with strong gaseous absorption, which is what is being looked for.

The majority of the comparisons of reflectivity were summarized by using the Minnaert function to fit the reflectivity of Oval BA as a function of the cosine of the incident and emission angles. This was important because individual measurements of Oval BA when it was white and when it was red never matched with identical values of the incident and emission angles.

The results of these fits are plotted using a linear fit of the Minnaert function described above in Equations 1 and 2. The logarithmic form (Eq. 2) is what is plotted in Figures 12-20. After all the data are plotted for each wavelength, a line of best fit is generated with uncertainty values for its slope and y-intercept for the values corresponding to both red and white epochs. Then, these two lines are overlaid against each other to be able to compare their respective observed μ*I/F values relative to each other.

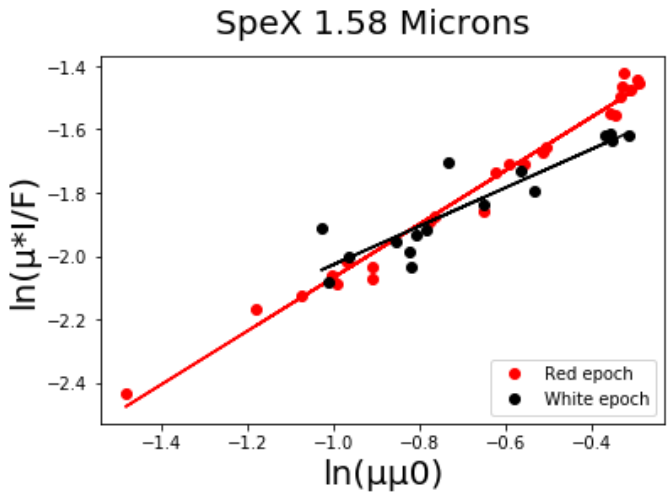


```
Red Slope: 0.84641779± 0.02421844
Red Y-Intercept: -1.22131399± 0.0180685
Red I/F: [0.25679519, 0.270026]

White Slope: 0.6088474± 0.07498217
White Y-Intercept: -1.41810073± 0.05436896
White I/F: [0.21390657, 0.249989]
```

Figure 12. A plot of the reflectivity as a function of emission and incident angles of SpeX observations of both the red and white epochs overlaid against each other at 1.58 μm (methane_short filter). The x-axis represents the logarithm of product of the emission and incident angle cosines and the y-axis represents the logarithm of the product of the reflectivity at that angle times the emission-angle cosine. Values for the slope and intercept of the fit are shown together with their respective uncertainties, along with the I/F range representing the confidence interval *at the maximum value of the product of μ and* μ_0.

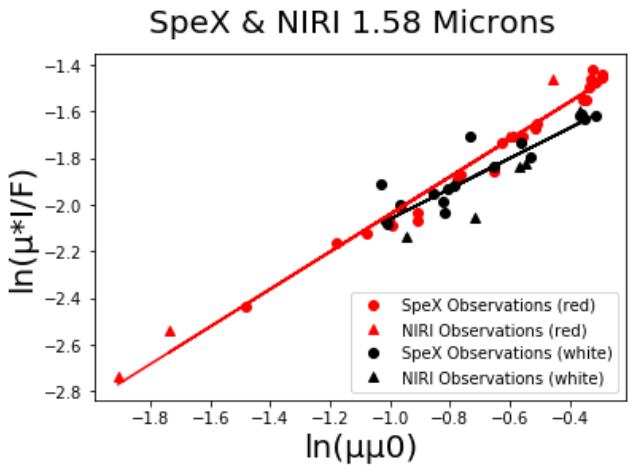

Red Slope: 0.80229419±0.02332903
Red Y-Intercept: -1.23881124± 0.02000795
Red I/F: [0.25517426, 0.269225]

White Slope: 0.65093968± 0.08001713
White Y-Intercept: -1.41109271± 0.05680945
White I/F: [0.21172591, 0.24944]

Figure 13. A plot of the same data as in Fig. 12 but with the combination of NIRI and SpeX measurements.

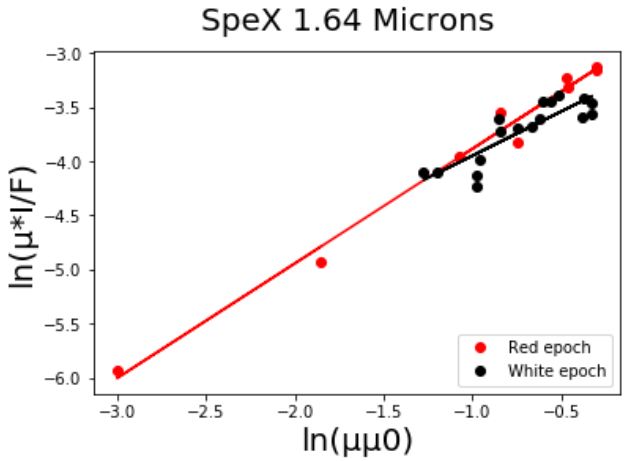

Red Slope: 1.06082916± 0.04928986
Red Y-Intercept: -2.82302855± 0.06463393
Red I/F: [0.045391, 0.053219]

White Slope: 0.81848166± 0.12689848
White Y-Intercept: -3.12862899± 0.09817754
White I/F: [0.03385951, 0.04477715]

*Figure 14. A plot of values similar to Figure 12, but for 1.64 μm (*iron II*).*

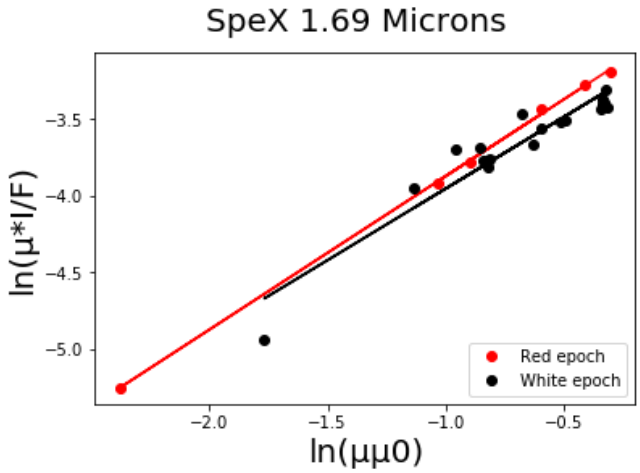

Red Slope: 1.00397857± 0.01396278
Red Y-Intercept:-2.86757961 ± 0.0162671
Red I/F: [0.0471562, 0.049133]

White Slope: 0.93642479± 0.07514545
White Y-Intercept: -3.0166372± 0.05770462
White I/F: [0.03878209, 0.045651]

Figure 15. A plot of values similar to Figure 12, but for 1.69 μm (methane_long filter).

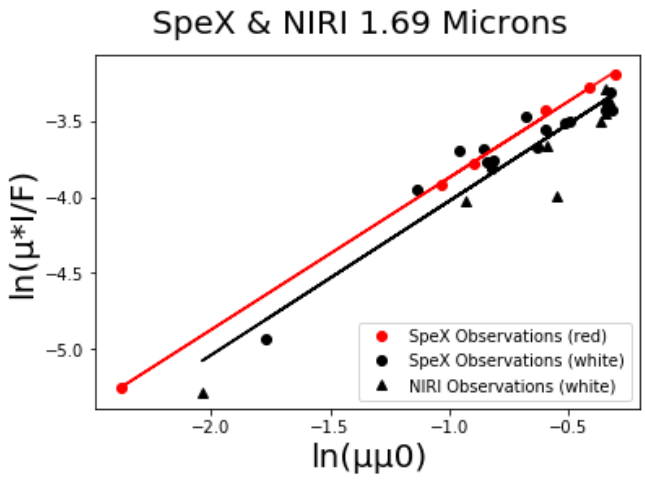

Red Slope: 1.00397857± 0.01396278
Red Y-Intercept:-2.86757961 ± 0.0162671
Red I/F: [0.0471562, 0.049133]

White Slope: 1.01628559± 0.0700657
White Y-Intercept-3.00958499± 0.05703948
White I/F: [0.03816652, 0.044723]

Figure 16. A plot of values similar to Figure 13, but for 1.69 μm (methane_long filter).

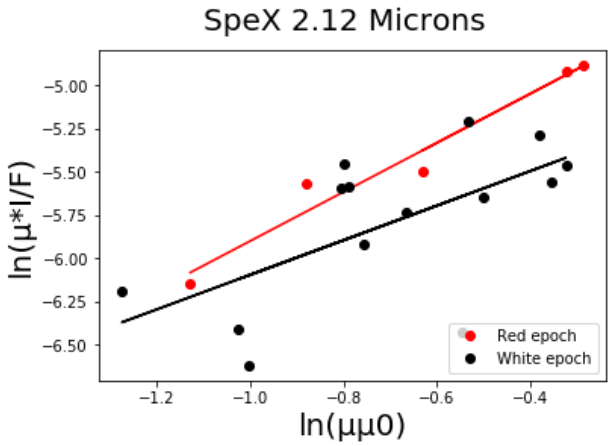

Red Slope: 1.42600573± 0.17389225
Red Y-Intercept: -4.4765554± 0.12617675
Red I/F: [0.007229, 0.01029]

White Slope: 1.00432517± 0.36469462
White Y-Intercept: -5.09312947± 0.27242739
White I/F: [0.003491, 0.007631]

Figure 17. A plot of values similar to Figure 12, but for 2.12 μm (H_2 1-0 filter).

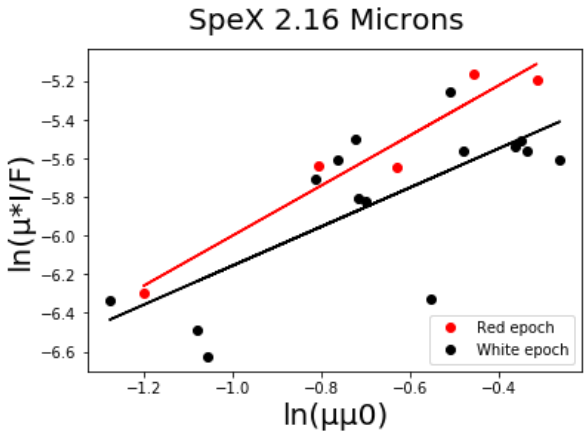

Red Slope: 1.29598698± 0.19718198
Red Y-Intercept: -4.70374829± 0.14747455
Red I/F: [0.00558296, 0.008489]

White Slope: 1.01067318± 0.2637717
White Y-Intercept: -5.14465411± 0.19168533
White I/F: [0.00391525, 0.006599]

*Figure 18. A plot of values similar to Figure 12, but for 2.16 μm (*bracket_gamma filter*).*

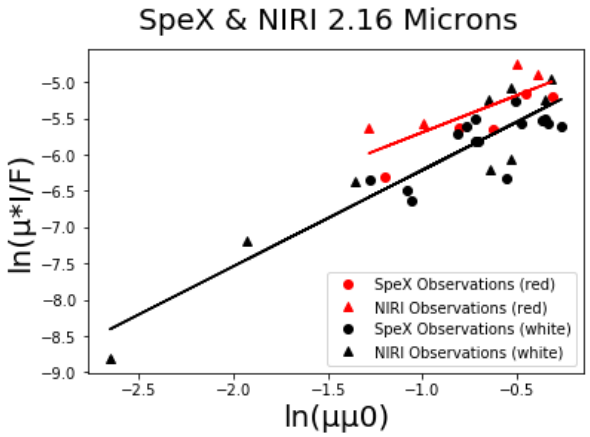


```
Red Slope: 1.02041088± 0.31069051
Red Y-Intercept: -4.67276538± 0.25043442
Red I/F: [0.00546698, 0.010969]

White Slope: 1.32781995± 0.13152863
White Y-Intercept: -4.8856821± 0.12628794
White I/F: [0.00515853, 0.007116]
```

*Figure 19. A plot of values similar to Figure 13, but for 2.16 μm (*bracket_gamma filter*).*

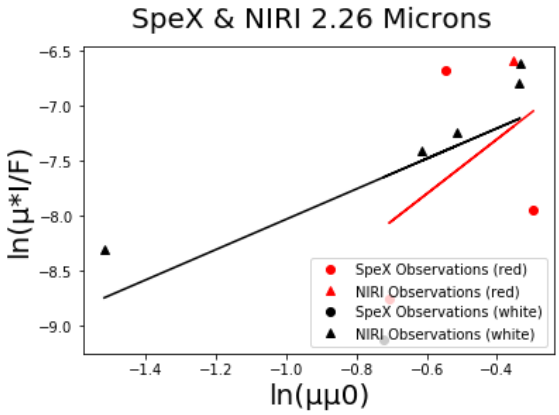


```
Red Slope: 2.47980977± 3.5342026
Red Y-Intercept: -6.31110439 ± 1.77739889
Red I/F: [0.0000595766662, 0.0169554478]

White Slope: 1.37737603± 0.84091832
White Y-Intercept: -6.65247352± 0.65965546
White I/F: [0.000373, 0.002448]
```

*Figure 20. A plot of values similar to Figure 13, but for 2.26 μm (*continuum-K*).*

Conclusions

At 1.58 μm, tropospheric water-ammonia clouds are detectable at pressures greater than or equal to 700 mbar. Reflectivity at this wavelength is sensitive to the reflectivity of the cloud particles. The confidence interval for the observed reflectivity for the red epoch of the combined SpeX and NIRI observations is [0.25517426, 0.269225] and for the white epoch is [0.21172591, 0.24944]. Thus, there is a small but still significant difference between the two epochs at this wavelength that is evident at the highest values of $\ln(\mu\mu_0)$. So, it can be concluded that there exists a change in observed reflectivity in correlation to the color change of Oval BA in the 1.58-micron filter.

The 1.64- and 1.69-μm filters sense regions of intermediate gaseous absorption. At these wavelengths, high tropospheric haze cloud particles are detectable near 200 mbars of pressure. At low emission angles (high x-axis values) at these wavelengths, the y-values for the red epoch are consistently higher

than the y values for the white epoch. The confidence interval for the observed reflectivity for the red epoch at 1.64 microns is [0.045391, 0.053219] and for the white epoch is [0.03385951, 0.04477715]. Once again, there is no overlap in confidence intervals. The confidence interval for the observed reflectivity for the red epoch of combined SpeX and NIRI observations at 1.69 µm is [0.0471562, 0.049133] and for the white epoch is [0.03816652, 0.044723]. There is a huge difference in confidence intervals. Hence, there is a difference between the two epochs at 1.69 microns. Therefore, the white epoch of Oval BA has a lower reflectivity of high-altitude hazes, implying that in the white epoch, Oval BA's clouds are lower in altitude compared to its red epoch.

The 2.12- and 2.16-µm filters sense stronger gaseous absorption and are sensitive to particles even higher – in the lower stratosphere around 80-100 mbars of pressure. The confidence interval at 2.12 µm SpeX for the red epoch is [0.007229, 0.01029] and for the white epoch is [0.003491, 0.007631]. Since there is small but still considerable overlap between these two intervals, it cannot be concluded that there exists a change in reflectivity at this filter. The confidence interval at 2.16 microns combined SpeX and NIRI for the red epoch is [0.00546698, 0.010969] and for the white epoch is [0.00515853, 0.007116]. Once again, since there is significant overlap between these two intervals, it cannot be concluded that there exists a change in reflectivity at the 2.16-micron filter. The same holds good for 2.26 µm. Thus, we do not know if a change occurred in the vertical distribution of haze particles in Oval BA during its red to white transition in the lower stratosphere.

To summarize, as a result of Oval BA's color change from red to white, Oval BA has different cloud properties in the upper troposphere, roughly at 200 mbar of pressure or more but not in the lower stratosphere at pressures of 80-100 mbar.

Acknowledgments

Thank you to mentor Glenn Orton and co-mentor Thomas Momary at the Jet Propulsion Laboratory, California Institute of Technology for their guidance and support in this research. Thank you to JPL Visiting Student Research Program and JPL Education Office - Student & Faculty Programs for the opportunity. Thank you to Naveen Foundation for funding me. Thank you to Internship Office of Coimbatore Institute of Technology for their help during on-boarding. Lastly, thank you to everyone who has provided support and guidance for the research.

References

[1] Baines, K. H., R. A. West, L. P. Giver, and F. Moreno. 1993. Quasi-random narrow band model fits to near-infrared low-temperature laboratory methane spectra and derived exponential-sum absorption coefficients. J. Geophys. Res. - Planets 98, E3, 5517-5529.

[2] Reuter, D. C., A. A. Simon-Miller, A. Lunsford, K. H. Baines, A. F. Cheng, D. E. Jennings, C. B. Olkin, J. R. Spencer, S. A. Stern, H. A. Weaver, and L. A. Young. 2007. Jupiter cloud composition, stratification, convection, and wave motion: A view from New Horizons. Science 318, 223-225.

[3] Irwin, P.G.J., N.A. Teanby, R. de Kok, L.N. Fletcher, C.J.A. Howett, C.C.C. Tsang, C.F. Wilson, S.B. Calcutt, C.A. Nixon, P.D. Parrish. 2008. The NEMESIS planetary atmosphere radiative transfer and retrieval tool, J. Quant. Spectrosc. and Rad. Trans., 109, 1136-1150.

[4] Irwin, P.G.J., Dobinson, J, James A, Toledo D, Teanby N.A., Fletcher, L.N., Orton G.S., Perez -Hoyos, S. Latitudinal variation of methane abundance above 2 clouds in Neptune's atmosphere from 3 VLT/MUSE-NFM: Limb-darkening reanalysis. Icarus